Article

Not peer-reviewed version

TPA and PET Photo-Degradation by Heterogeneous Catalysis Using a $(Al_2O_3)_{0.75}TiO_2$ Coating

Mónica A. Camacho-González , Alberto Hernández-Reyes , Aristeo Garrido-Hernández , Octavio Olivares-Xometl , Natalya V. Likhanova , Irina V. Lijanova *

Posted Date: 27 March 2025

doi: 10.20944/preprints202503.2121.v1

Keywords: TPA; PET; photo-degradation; heterogeneous catalysis

 doi:10.20944/preprints202503.2121.v1

Article

TPA and PET Photo-Degradation by Heterogeneous Catalysis Using a $(Al_2O_3)_{0.75}TiO_2$ Coating

Mónica A. Camacho-González [1], Alberto Hernández-Reyes [1], Aristeo Garrido-Hernández [2], Octavio Olivares-Xometl [3], Natalya V. Likhanova [4] and Irina V. Lijanova [1,*]

[1] Instituto Politécnico Nacional, Centro de Innovación e Investigación Tecnológica, Cerrada Cecati S/N, Colonia Santa Catarina de Azcapotzalco, CDMX 02250, México
[2] Universidad Autónoma Metropolitana, Departamento de Materiales, Av. San Pablo 420, Col. Nueva el Rosario, Azcapotzalco, CDMX 02128, México
[3] Benemérita Universidad Autónoma de Puebla, Facultad de Ingeniería Química, Av. San Claudio y 18 Sur, Ciudad Universitaria, Col. San Manuel, Puebla 72570, México
[4] Instituto Mexicano del Petróleo, Eje Central Norte Lázaro Cárdenas No. 152, Col. San Bartolo Atepehuacan, G. A. Madero, CDMX 07730, México
* Correspondence: ivictorvnal@ipn.mx

Abstract: The combination of the catalytic properties of Al_2O_3/TiO_2 formed an efficient system to degrade the ubiquitous pollutants TPA and PET. The coating $(Al_2O_3)_{0.75}TiO_2$ was characterized by X-ray diffraction. Stainless steel disks with photo-catalyst coating were placed transversely in a 3.0-L vertical glass reactor with ascending airflow for supplying oxygen to the reaction medium and visible light lamps for photo-activation. The analysis of the coating homogeneity, morphology and particle size distribution of the TiO_2 coatings and $(Al_2O_3)_{0.75}TiO_2$ system were confirmed by SEM. Optical properties and band-gap energy were calculated by using the Tauc equation. UV-Vis spectrophotometry (UV-Vis) and chemical oxygen demand (COD) were the quantitative techniques to measure the reduction of the initial TPA and PET concentrations.

Keywords: TPA; PET; Photo-degradation; Heterogeneous Catalysis

---

Graphical Abstract

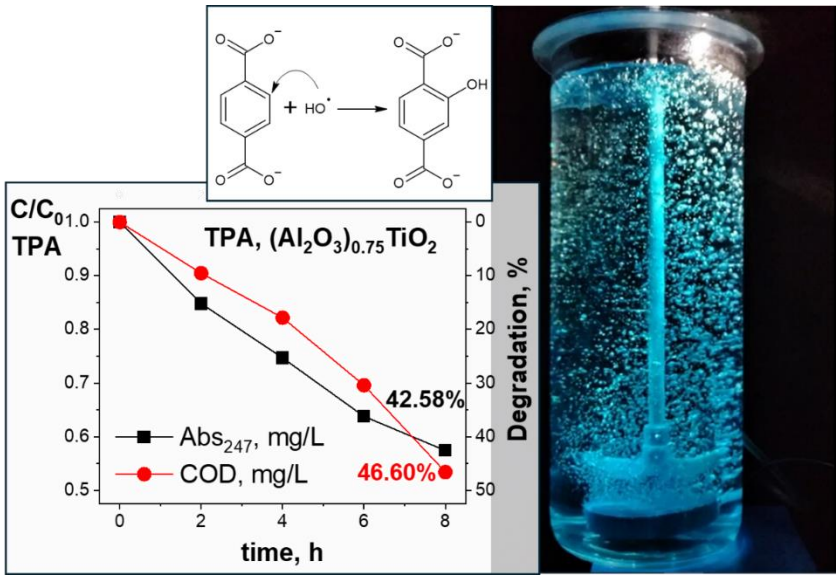

1. Introduction

 doi:10.20944/preprints202503.2121.v1

Polyethylene terephthalate (PET) is the most widely used thermoplastic polymer in various areas due to its application diversity, as well as to its strength, lightness, elasticity and transparency properties (Peng et al., 2023). In contrast, its degradation rate is low by acid or basic hydrolysis, methanolysis, glycolysis and acetolysis, which are chemical methods that can depolymerize PET into monomers such as terephthalic acid, ethylene glycol diacetate, colorants and special additives (Fang et al., 2018; Kurokawa et al., 2003). Terephthalic acid (TPA) or 1,4-benzene dicarboxylic acid is the final product of successive oxidation reactions of p-xylene, serving as a raw material in the manufacture of PET and other plastics, dyes, perfumes, pesticides, medicines, etc. (Thiruvenkatachari et al., 2007; Xiao et al., 2010). Wastewater discharged from the production of PET and TPA has high concentration of different carboxylic acids like para-toluic, benzoic, acetic, phthalic, isophthalic and excess of terephthalic (K. Ma et al., 2020). Due to the high stability of the aromatic structure, terephthalic acid is a ubiquitous pollutant in sediments, natural waters, soils, aquatic organisms, etc. (Billings et al., 2021); TPA resists degradation by aerobic, anaerobic, and combined biological means and electrocoagulation (Chang et al., 2004; Kleerebezem et al., 2005; K. Ma et al., 2020; Sannino et al., 2021; Yan et al., 2004). In addition, TPA exerts an inhibitory effect on the growth of microorganisms, drastically decreasing the biomass during the degradation processes and extending the treatment period (Li et al., 2022). The refining process includes a neutralization reaction with alkalis, which produces an excessive amount of salt and substantially reduces the efficiency or sometimes prevents anaerobic treatment (X. Ma et al., 2020; Muñoz Sierra et al., 2017; H. Zhang et al., 2022).

Recently, advanced oxidation processes (AOPs) have become more common for the effective decomposition of organic matter in wastewater, including photocatalytic oxidation (UV-TiO_2), ozonation, and Fenton oxidation (H_2O_2-Fe) (Gogate & Pandit, 2004; Kaneco et al., 2004; Mazzarino & Piccinini, 1999). AOPs proceed by generating super-reactive free radicals, which oxidize organic pollutants into less harmful or short-chain structures, which could be treated by biological means (Park et al., 2003). It should be emphasized that the symmetrical position of substituent groups in the aromatic ring of TPA improves its structural stability, which is widely used to detect $\bullet OH^-$ radicals generated in photocatalytic processes aiming to evaluate the effectiveness of various photocatalysts (Žerjav et al., 2020). The degradation of TPA, desirably, must happen by means of non-toxic solid heterogeneous photocatalysts at ambient temperature and pressure, with the removal of multiple compounds from wastewater (Jiang et al., 2022; Sacco et al., 2018). Therefore, the main challenge of AOPs is the design of an ideal photocatalyst with speedy-oxidizing power under radiation, high chemical and photo stability, low cost and high availability (Merino et al., 2016). Environmentally friendly TiO_2 is the most promising UV-photocatalyst with wide bandgap (anatase, 3.2 eV) and acceptable recombination of photogenerated electrons. The activation of TiO_2 by visible light could be promoted by doping it with different elements such as nickel, platinum, copper, etc. and metal oxides like ZnO, WO_3, and Al_2O_3 to generate hetero-structures that work as a traps for photo-generated electrons, shifting the absorption of TiO_2 to the visible spectrum (Al Miad et al., 2024; Byrne et al., 2018; Krishnan et al., 2024; Ran et al., 2023; Wang et al., 2024).

The enhancement of the photocatalytic activity of mixed oxides under UV and visible radiation was shown by Al_2O_3-TiO_2 in suspension or as thin films, in comparison with austere TiO_2 without doping (Karunakaran et al., 2015; Yakdoumi & Hadj-Hamou, 2020; Q. Zhang et al., 2016). The combination of the catalytic properties of TiO_2 and the relevant mechanical resistance, high chemical and thermal stability and adsorption capacity of Al_2O_3 gives the system potential reusability without losing efficiency to degrade pollutants (Magnone et al., 2021; Martinez-Gómez et al., 2022). In specialized wastewater treatment, immobilized photocatalysts could help skip the filtration step at the end of the process; however, reducing the surface/volume ratio causes slow mass transfer and less availability of catalytically active sites (Kanakaraju et al., 2014; Y. Zhu et al., 2022). Regardless of the nature of the photocatalyst, the design of reactors for the photocatalytic degradation of organic pollutants in aqueous solution is an area in constant development (W. Zhang et al., 2011). However, there are three fundamental limitations of a photocatalytic process: a) mass transport, b) efficient

 doi:10.20944/preprints202503.2121.v1

propagation of photons to the photocatalyst and c) the amount of molecular oxygen dissolved in a solution (Duan et al., 2020; Ibarra et al., 2020; Samy et al., 2021).

In this study, the purpose was to evaluate the efficiency of Al_2O_3-TiO_2 photocatalyst coatings deposited on 304 stainless steel (304 SS) perforated discs by the dip-coating technique to degrade TPA and PET by heterogeneous photocatalysis. The disks with photocatalyst coating were placed transversely in a 3.0-L vertical glass reactor with ascending air flow to supply oxygen to the reaction medium and visible light lamps for photo-activation. UV-vis spectrophotometry and chemical oxygen demand were the quantitative techniques employed to measure the reduction of the initial TPA and PET concentrations.

2. Materials and Methods

2.1. Coating Preparation by the Sol-Gel Route

The $(Al_2O_3)_{0.75}TiO_2$ photocatalyst was obtained by the sol-gel and dip-coating techniques from precursor solutions of aluminum sulfate $[Al_2(SO_4)_3]\cdot 18H_2O$ (Meyer, CDMX, Mexico, 98%) and titanium tert-butoxide TBT (Sigma Aldrich, St. Louis, MI, USA, 97%). According to the methodology, (Camacho-González et al., 2023) a 1 M NaOH (Meyer, CDMX, Mexico, ≥ 97%) solution was added dropwise to 95 mL of a 0.1 M $[Al_2(SO_4)_3]\cdot 12H_2O$ solution until pH=10; the obtained colloidal suspension was kept under stirring at 70 °C for 5 h. Afterward, the suspension was washed three times with an ethanol/water (50:50 v/v) solution to remove SO_4^{2-} ions. The wet solid was redispersed in 50 mL of ethanol (Sigma Aldrich, St. Louis, MI, USA, 99.9%); this suspension was aged for 24 h. Four hours before the end of the aging period of the aluminum suspension, 25 mL of a 0.3 M HNO_3 (Meyer, CDMX, Mexico, 65%) solution were added dropwise to 30 mL of a TBT/ethanol (15% v/v) solution; the suspension was stirred for 2 h to achieve the completion of the hydrolysis–condensation reaction. Hereafter, the aluminum suspension was added to the forming $[TiO(OH)_2]_n$ gel and kept under vigorous stirring until a white milky colloidal suspension appeared. Meanwhile, five circular AISI 304 SS disks with diameters of 104 mm and orifice diameters of 2 mm were washed with non-ionic detergent soap, followed by an acetone washing in a sonication bath at 400 kHz for 20 min to eliminate oil traces, and stored in isopropyl alcohol for 1 h. Subsequently, the disks were immersed in the milky colloidal suspension of aluminum-titanium hydroxides and withdrawn at 40 mm/min. After each immersion, the disks were dried at 80 °C for 1 h; in the last of the three depositions after the treatment at 80 °C, they were treated at 180 °C for 1 h and, finally, annealed at 700 °C for 5 h. Five 304 SS disks with TiO_2 coatings were obtained by the same technique without mixing with the 0.1 M $[Al_2(SO_4)_3]\cdot 12H_2O$ solution.

2.2. Structural Characterization Measurements

The structural study of the $(Al_2O_3)_{0.75}TiO_2$ photocatalyst was carried out first, with a Bruker Diffractometer D8 Advance using Cu Kα radiation (1.54184 Å), room temperature and 2θ angle ranging from 20° to 80° with 0.02 s^{-1} pulse to determine the crystallinity and crystal phase of the produced coating. Rietveld refinement was performed with Profex, version 5.2.3. The statistical values were Rwp = 40.47, Rexp = 3.77, X2 = 1.57, and a goodness-of-fit (GoF) score of 1.25. The analysis of the morphology and size of the particles was performed by employing a field emission scanning electron microscope (FE-SEM) Hitachi SU5000; for the EDS analysis, a coupled Bruker Quantax XFlash 6/60 was used to investigate the compositional aspects of the coating. The optical characteristics of the $(Al_2O_3)_{0.75}TiO_2$ coating were examined by a Perkin Elmer model Lambda 35 UV-vis spectrophotometer from 200- to 900-nm wavelength to register absorbance values of the coating scratch. The bandgap energy was obtained using the Tauc Equation (1), which relates the absorption coefficient to the energy of incident radiation and bandgap. The intersection of the linear part of the curve $(\alpha \cdot E)^r$ vs. E with the x-axis represents $(\alpha \cdot E)^r$=0, therefore, $E - E_g$ (Barajas-Ledesma et al., 2010):

$$(\alpha \cdot E)^r = Ai\left(E - E_g\right) \qquad (1)$$

 doi:10.20944/preprints202503.2121.v1

where α is the absorbance in arbitrary units; E is the photon energy in eV; Ai is a proportionality constant in eV; Eg is the bandgap in eV, and r is a coefficient that classifies indirect allowed transitions (r = 2), direct allowed transitions (r = 1/2), direct forbidden transitions (r = 3/2), and indirect forbidden transitions (r = 3).

2.3. Photocatalytic Degradation

A 3-L cylindrical reactor was designed to measure all the degradation reactions. It was made of 4-mm thick low Fe borosilicate glass, with internal diameter and height of 111.2 and 312 mm and top lid of the same material and diameter with 4 inlets; ascending air flow and mechanical stirring were employed. Through the top central inlet, a CPVC pipe was passed, which in addition to protect the propeller rod, served as a guide for the five disks with $(Al_2O_3)_{0.75}TiO_2$ coatings (~215 cm^2 of coating area and 44±5 mg of photocatalyst per substrate) placed in a transverse position in the reactor. Five 304 SS disks with a diameter of 107 mm and thickness of 2 mm with $(Al_2O_3)_{0.75}TiO_2$ coatings were separated 40 mm from each other by a ¾-inch CPVC pipe placed in a transverse position, Figure 1a. In one of the lid inlets, a PP pipe was introduced to take 25 mL of solution at each time interval to quantify the COD (NMX-AA-030/2-SCFI-2011) in a HACH spectrophotometer, DR2010 (USA, Loveland, Colorado). In another inlet, a probe was introduced to measure the average pH (9.5±0.2) and temperature (30±0.5 °C). Eight Phillips LED lamps (4 W, 400 lumens, MR16 with emission within a 410–760 nm interval with a maximum peak at around 600 nm) were placed at 20 mm of the external wall reactor in pairs at 90 degrees to the center of the reactor for visible light irradiation, Figures 1b,c. A black box covered the reactor and lamps to avoid external radiation.

In the reactor, 50 mg/L of TPA dissolved in 2.5 L of a 0.1% NaOH solution were homogenized by upward airflow at 5 L/min with mechanical stirring for 30 min in the absence of light to allow adsorption-desorption equilibrium between the surface of the $(Al_2O_3)_{0.75}TiO_2$ coatings and contaminant. Subsequently, 25 mL of solution were extracted with a syringe to determine the initial TPA concentration as COD (mg/L) immediately after the lamps were lit. Every 2 h, the same volume of solution was collected to determine the COD (mg/L). The same methodology was applied for TPA degradation with TiO_2 coatings and PET degradation using $(Al_2O_3)_{0.75}TiO_2$. Each determination was performed in triplicate. Finally, the procedure was carried out under the same conditions to degrade PET using $(Al_2O_3)_{0.75}TiO_2$. The degradation experiments were carried out in triplicate.

The efficiency of the degradation of TPA and PET was calculated with Equation (2):

$$\%\ \boldsymbol{degradation} = \frac{\boldsymbol{COD_o - COD_t}}{\boldsymbol{COD_o}} \boldsymbol{x100} \qquad (\mathbf{2})$$

where COD_o is the initial concentration as COD of each contaminant before turning on the lamps, and COD_t is the concentration of the contaminant after time t.

 doi:10.20944/preprints202503.2121.v1

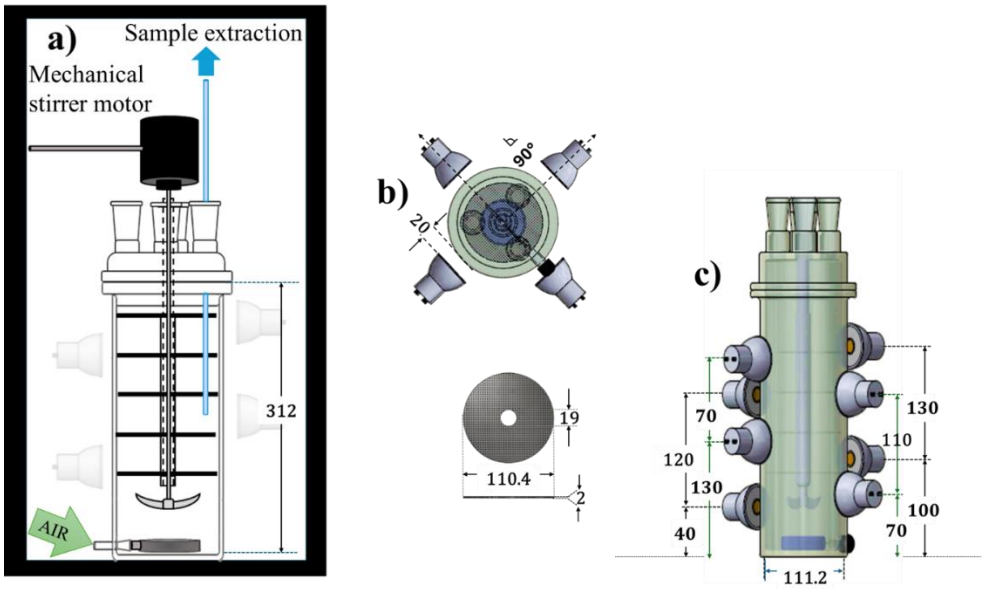

Figure 1. Airlift reactor, a) arrangement of 304 SS disks with $(Al_2O_3)_{0.75}TiO_2$ coatings, b) top view of the arrangement of lamps, and 304 SS disks; c) placement of lamps. The numbers correspond to lengths in millimeters.

3. Results and Discussion

3.1.(. $Al_2O_3)_{0.75}TiO_2$ Coating Characterization

3.1.1. X-Ray Diffraction

The XRD patterns of the synthesized TiO_2, Al_2O_3, and $(Al_2O_3)_xTiO_2$ oxide system powders in Figure 2 indicate that the synthesized TiO_2 exhibits predominantly the rutile phase, determined by the presence of the (110), (011), (020), (111), (120), (220), (002), (130) and (031) planes at 27. 45°, 36.1°, 39.2°, 41.3°, 44.0°, 56.6°, 63°, 64.0° and 69.06°, and 76.1°, respectively (Habibi & Jamshidi, 2020). According to the ICSD chart 98-008-2085, above 500 °C, the first peak of the (110) plane characteristic of rutile appears at 27.5 °, and near 700 °C, the anatase phase is completely transformed into rutile, being the most predominant stable phase (Farhadian Azizi & Bagheri-Mohagheghi, 2013).

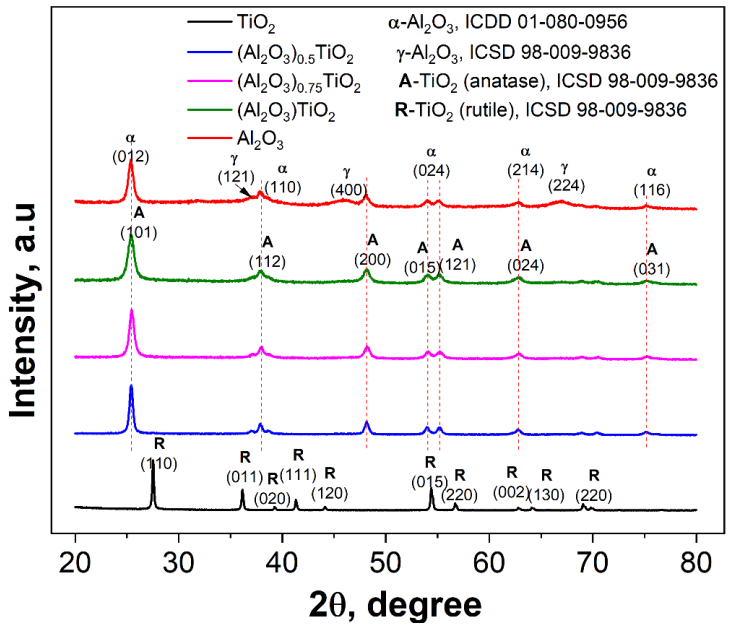

Figure 2. Diffraction X rays of $(Al_2O_3)_{0.75}TiO_2$ coating powders.

 doi:10.20944/preprints202503.2121.v1

In the case of the synthesized Al_2O_3, the presence of the planes (012), (110), (024), (214), and (116) is associated with the α-Al_2O_3 phase according to the ICDD chart 01-080-0956. The γ-Al_2O_3 phase is represented by the (121), (400), and (224) planes indicated in the ICSD chart 98-009-9836. The presence of the two phases is due to the transformation of boehmite AlO(OH) into α-Al_2O_3 and even γ- Al_2O_3 was promoted by the synthesis route and heat treatment at 400-700 °C (Sadeq et al., 2019; Xu et al., 2012; L. Zhu et al., 2017).

The protective layers of chromium oxide and magnetite formed on the surface of 304 SS during the high temperature treatment (near 800°C) were detected through the structural analysis of the coating (Askeland & Wright, 1998). The Cr atoms could diffuse toward the grain boundaries, forming voids through which the Fe atoms in the 304 SS matrix could migrate and react with oxygen from the atmosphere or residual oxygen in the chromium-rich magnetite system: $Fe^{2+}(Fe^{3+}, Cr^{3+})_2O_4$ (Miglierini et al., 2019; X. Zhang et al., 2020). Figure 3 shows the diffraction planes of stainless-steel disks in the absence of coating, without heat treatment, and with heat treatment at 700°C, 5 h observing this phenomenon in more detail.

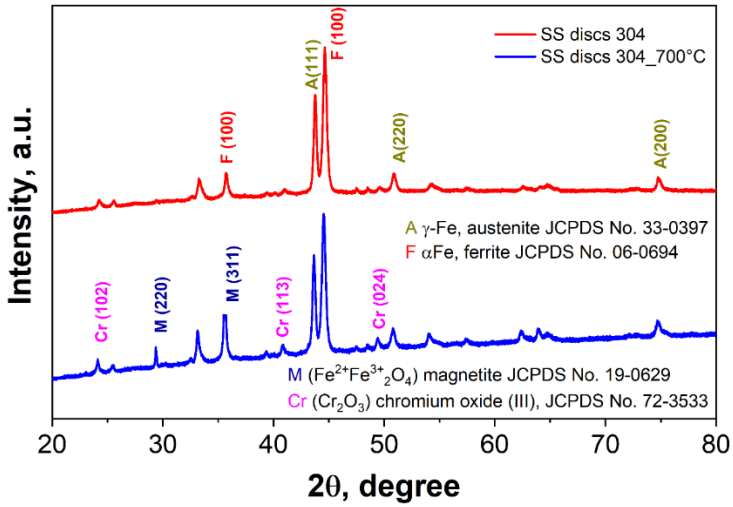

Figure 3. 304 SS disks with and without thermal treatment.

The Rietveld refinement method (Table 1) showed the phase composition of the $(Al_2O_3)_{0.75}TiO_2$ coating powders, percentages of components and lattice parameters. The quantification of the phases indicates that α-Al_2O_3 (35.0%) is more abundant than γ-Al_2O_3 (14.3%), while for TiO_2, the anatase phase present at 32.8% doubles the rutile phase with only 17.6%. The migration of Fe and Cr atoms to the grain surface happens due to the sensitization process of austenitic stainless steels during possible oxidation in the presence of oxygen, so, the same kind of covalent-coordination bonds: Fe-O-Al, Fe-O-Ti, Cr-O-Al and Cr-O-Ti are formed (Tian et al., 2014).

Table 1. Composition of $(Al_2O_3)_{0.75}TiO_2$ coating powders. Rietveld method.

Phase	%	Lattice parameters (nm)		
		a	b	c
$\alpha - Al_2O_3$	35.0	0.4748	–	1.294
$\gamma - Al_2O_3$	14.3	0.8017	–	–
TiO_2 $(anatase)$	32.8	0.3801	–	0.9595
TiO_2 $(rutilo)$	17.6	0.4620	–	0.2958

3.1.2. Energy Dispersive Spectroscopy. Elemental Analysis

 doi:10.20944/preprints202503.2121.v1

Figure 4 shows the micrographs and mappings of the elemental analysis of TiO_2 and the $(Al_2O_3)_{0.75}TiO_2$ coating by the energy dispersive X-ray spectroscopy (EDS) technique. 304 SS is composed of approximately 65 -75% of Fe and alloying elements in the substrate were confirmed too: 18-20% of chromium and 8-12% of nickel, with traces of manganese (<2%), silicon (<2%), phosphorus (<0.045%) and sulfur (<0.03%), maintaining low carbon content (<0.03%) (da Trindade et al., 2018). In agreement with the XRD analysis, Figure 4-a shows the result of the sintering process (700 °C), where Fe (39.89%), Cr (10.4%) and Ni (3.83%) presented migration to the surface, forming the respective oxides on the TiO_2 coating surface.

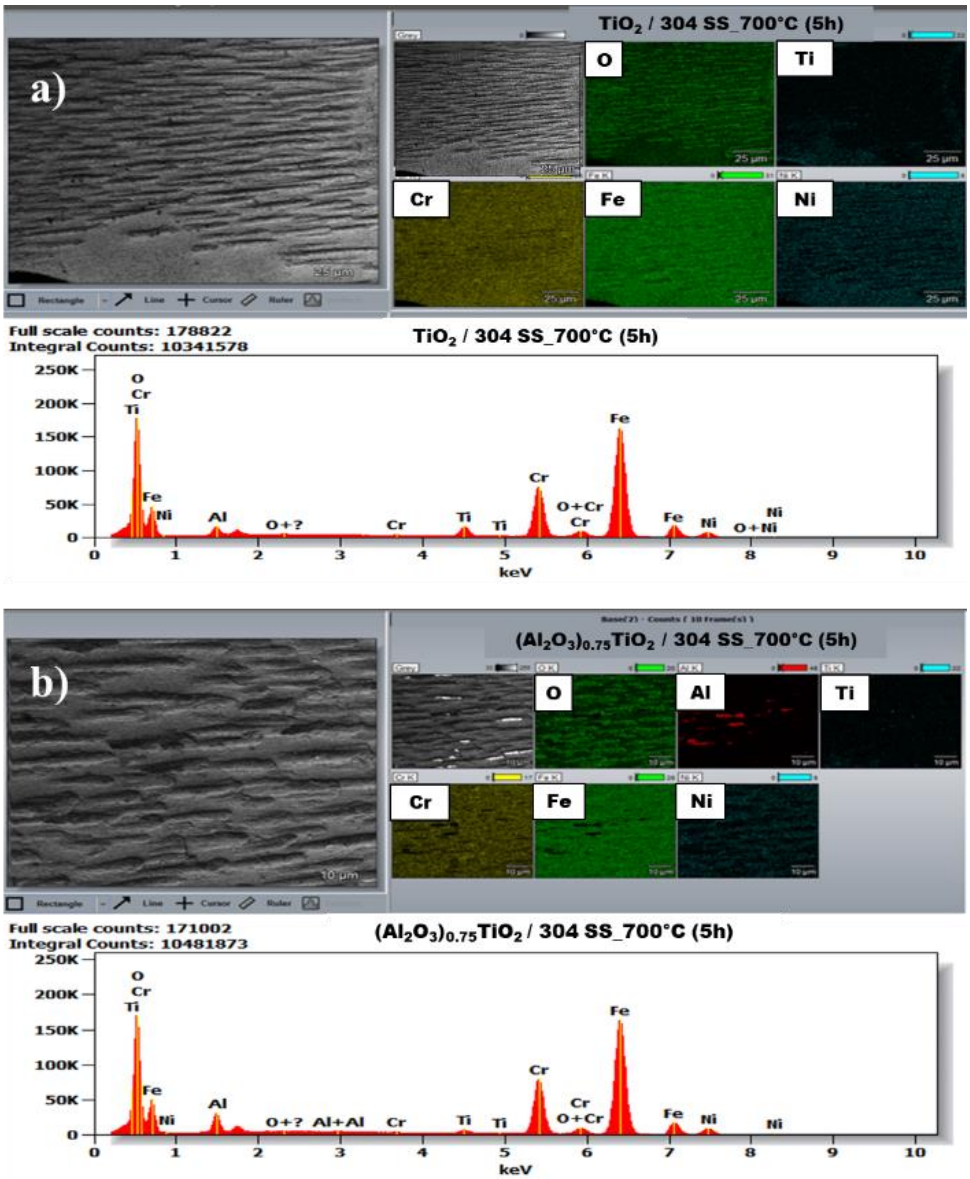

Figure 4. Micrographs and mapping of the elemental analysis of the coatings of a) TiO_2, area: 0.25 μm² magnification: 239 and, b) $(Al_2O_3)_{0.75}TiO_2$; area: 0.12 μm2, magnification: 478, deposited on 304 stainless steel. Resolution: 512 x 444 pixels, Voltage: 20.0 kV, detector: UltraDry.

Figure 4-b shows the homogeneous distribution of the $(Al_2O_3)_{0.75}TiO_2$ system, confirming the presence of Al (3.83%), Ti (2.62%) and the diffusion onto the surface of the formed Fe (32. 23%) and Cr (25.15%) oxides. The constant and homogeneous distribution of oxygen in mass percentage from 22.96 to 25.46% was associated with the formation of M-O bonds between the oxygen atoms present in the coating and the surface metal atoms (Oladijo et al., 2020).

3.1.3. Scanning Electron Microscopy. Morphology and Particle Size

 doi:10.20944/preprints202503.2121.v1

The analysis of the coating homogeneity, morphology and particle size distribution in the TiO_2 coatings and $(Al_2O_3)_{0.75}TiO_2$ system are shown in Figure 5; in both cases, the surface is homogeneously distributed, with no fractures, and delamination or uncoated areas are visible. For the TiO_2 coatings (Figure 5-a) on 304 stainless steel, deposits of spongy filamentous microstructures are observed whose mean length distribution is 240.7 ± 102 nm, 54% of the measured filaments are within the interval ranging from 200 to 300 nm (Figure 5-a'). Due to the independent nature of the oxides that formed the system and the synthesis conditions, two different and independent morphologies are observed for the $(Al_2O_3)_{0.75}TiO_2$ coating (Figure 5-b). The presence of spongy filamentous microstructures is related to TiO_2 as previously analyzed, while the formation of spherical agglomerated particles of the $(Al_2O_3)_{0.75}TiO_2$ coating may be associated with the presence of Al_2O_3 and the sintering temperature (Figure 5-b'). Liu and co-workers (Liu et al., 2023) synthesized TiO_2-SiO_2-Al_2O_3 composite coatings at different sintering temperatures on the surface of Q235 carbon steel by the sol-gel method to improve its corrosion resistance. As the authors increased the sintering temperature above 650 °C, the coating layer was composed of interlocked vine-shaped microstructures; in addition, the appearance of mesopores was observed. In the analysis, the various morphologies of the coating were attributed to the increase in coating components on the surface, among which, besides Al_2O_3, Fe_3O_4 and Cr_2O_3 stood out.

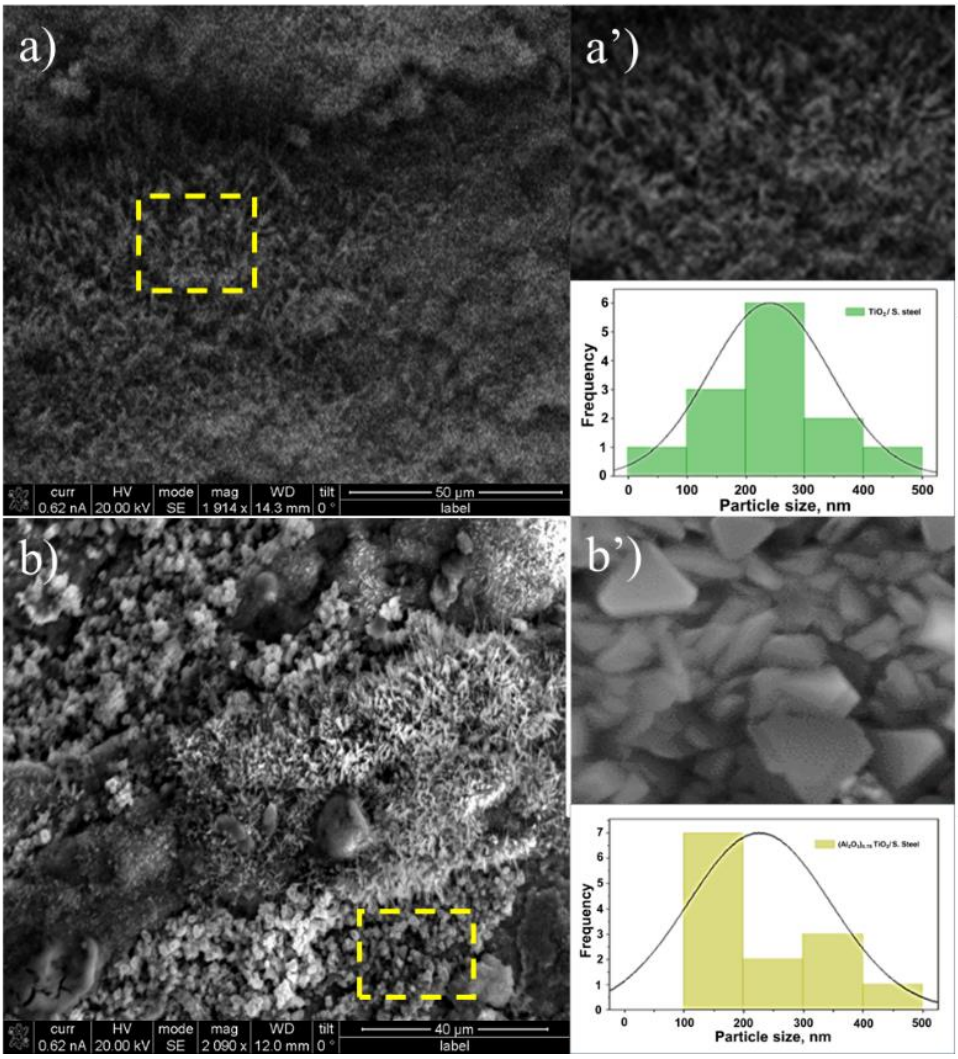

Figure 5. Micrographs of (a) TiO_2 coating on 304 stainless steel discs, a') magnification of the yellow zone of the TiO_2 coating and particle size distribution plots; b) $(Al_2O_3)_{0.75}TiO_2$ coating, b´) magnification of the yellow zone and particle size distribution plots.

 doi:10.20944/preprints202503.2121.v1

The spherical particle size distribution of the $(Al_2O_3)_{0.75}TiO_2$ coating was 226.3 ± 120 nm. It is visible that the heterogeneity of the particles deposited on the surface allows the formation of mesopores and high roughness surfaces that ensure a more efficient photocatalytic degradation process. In the sol-gel synthesis, during the formation of the sol, successive hydrolysis and condensation reactions gave rise to fractal aggregates, which successively joined, forming clusters whose expansion process brought the system to the solidification point or gel, changing the viscosity of the medium due to the rapid elimination of solvent. During aging, the phenomenon of syneresis (expulsion of liquid from the pores between clusters) occurred, and the successive thermal treatment caused the deformation of the polymeric network because of to the loss of liquid between the pores. The increase in capillary pressure reflected the shrinkage of the network, which resulted in dense agglomerated ceramics with high porosity and high surface area, making these materials ideal catalysts and support matrices (Brinker & Scherer, 2013).

3.1.4. UV-Visible Spectroscopy. Optical Properties and Determination of the Forbidden Band Energy

Figure 6-a shows the absorption of the $(Al_2O_3)_{0.75}TiO_2$ coating. The combined factors of the synthesis conditions, mainly the thermal treatment to which the oxide system was subjected with x=0.75 when depositing the disks, the thickness (250 ± 50 nm) and particle size distribution (226.3 ± 120 nm) favored a special spatial confinement.

Heat treatment at 700 °C promoted the sensitization of the 304 stainless steel substrates, which allowed the formation of Cr-rich carbide at the grain boundaries. Chromium in the carbide reacts with the surrounding oxygen, forming a passive chromium oxide layer. This migration can lead to interfacial interactions with the Al_2O_3 and TiO_2 phases of the coating, since both the coating structure and crystallization come from the same solution. It has been described in the literature that heterojunctions with carbonaceous materials, metal nanoparticles and metal oxides result in improved response in the visible spectrum and enhanced photocatalytic activity of TiO_2 (Huang et al., 2020; Liu et al., 2017; Sun et al., 2021).

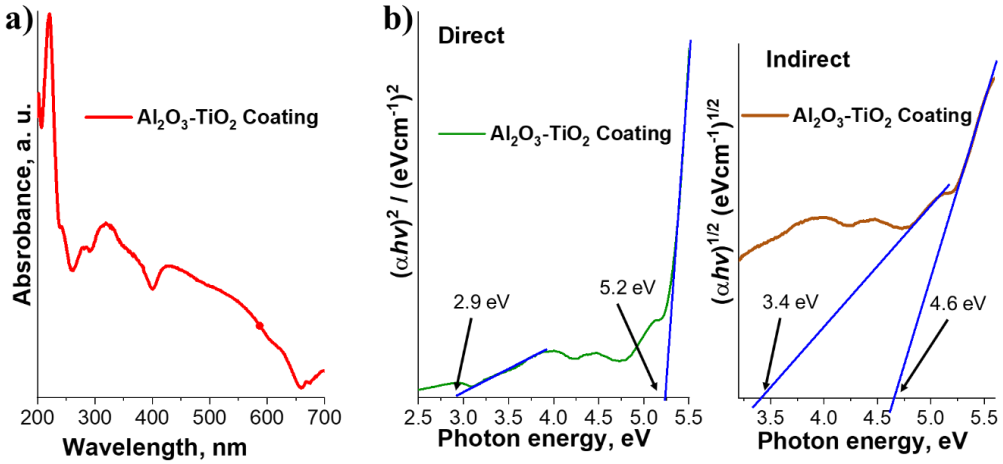

Figure 6. a) UV-Vis absorption spectrogram for the $(Al_2O_3)_{0.75}TiO_2$ coatings on stainless steel. b) Determination of the bandgap energy of the photocatalyst deposited on steel by the Tauc equation.

Figure 6-b shows the Tauc diagram of the $(Al_2O_3)_{0.75}TiO_2$ coating, where the calculation revealed forbidden band values of rutile (3.4 eV) and anatase (2.9 eV) corresponding to 2 TiO_2 phases; and the values of 4.6 and 5.2 eV were assigned to the α-Al_2O_3 and γ-Al_2O_3 phases (Luo et al., 2021; Mwema et al., 2018). It is necessary to indicate that the presence at low concentration of the pairing of two oxides, Cr_2O_3 with forbidden band of 3.15 eV (Kamari et al., 2019) and Fe_3O_4 with 2.7 eV (Radoń et al., 2017) with the $(Al_2O_3)_{0.75}TiO_2$ in the coating, considerably improved the absorption in the visible spectrum.

 doi:10.20944/preprints202503.2121.v1

3.2. Evaluation of the Photocatalytic Efficiency in the Degradation of Terephthalic Acid by the Immobilized $(Al_2O_3)_{0.75}TiO_2$ System

TPA exhibits characteristic absorption maxima at 190 nm, 241 nm and 285 nm when dissolved in an acidic medium (Kolesnik, 2024). The appearance of a weak absorption band between 280 and 290 nm, which shifts to shorter wavelengths, as the polarity of the solvent increases, indicates the presence of a carbonyl group. This type of shift, called "blue shift" or "hypsochromic", is related to the behavior of the chromophore. Likewise, an absorption band near 260 nm with fine vibrational structure is indicative of an aromatic ring (Skoog et al., 2008). Spectra in the UV region of aromatic hydrocarbons are characterized by three sets of bands originating from π→π* transitions. Figure 7 shows the TPA spectra from 200 to 300 nm at different photocatalytic degradation breakthrough times. For TPA dissolved in 0.1% NaOH, the absorption maxima occurred at 247 nm, where the band was blue-shifted, due to the basic nature of the solution. The bands at 229 and 242 nm were assigned to the π→π^* transitions of the sp^2 C=C conjugated bonds of the aromatic ring. Likewise, at 201-202 nm, the characteristic band of the carboxyl group with n→π^* transition type was observed.

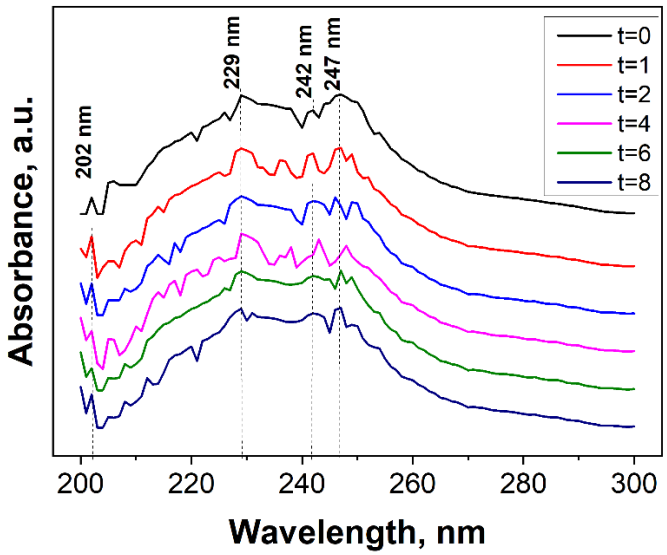

Figure 7. Monitoring of the UV-visible absorption during the photocatalytic degradation of TPA.

As the reactions elapsed at time t, the broad band near 247 nm split into two from the first hour of reaction, which could be associated with the binding of the photogenerated OH· radical to the aromatic ring, generating 2-hydroxy-terephthalic acid (Figure 7) (Zielińska-Jurek et al., 2015). This reaction can be associated with the attenuation of the band near 242 nm and the alternating appearance of a band near 235 nm. The band of the carboxyl group did not undergo apparent change and its conversion to CO_2 was minimal according to the 28.12% reduction of the absorbance value for this band (Agostini et al., 2022). The efficiency of photocatalytic oxidation (ZnO 2.5 g/L) of TPA reached 95%, where the operative parameters were: volume=1.5 L, pH=9.0, at 30°C, adding amounts of H_2O_2 as a scavenger of photogenerated electrons to produce $OH^{\bullet}$- radicals (Shafaei et al., 2010). Same studies reported that the degradation of the subsequent hydroxylation of TPA intermediates led to the cleavage of the aromatic ring, forming short-length carboxylic acids such as oxalic, formic, maleic, fumaric and acetic that are capable of reacting directly with hydroxyl radicals, finally being mineralized to CO_2 (Mahmoodi & Arami, 2006).

The degradation efficiency of TPA employing TiO_2 coatings on 304 SS steel discs was 28.39% (red line), measured from the remaining concentration by absorbance at 247 nm, and 30.63% (blue line), measured by residual concentration measurement as COD, with a difference between both techniques of 1.24% (Figure 8a).

 doi:10.20944/preprints202503.2121.v1

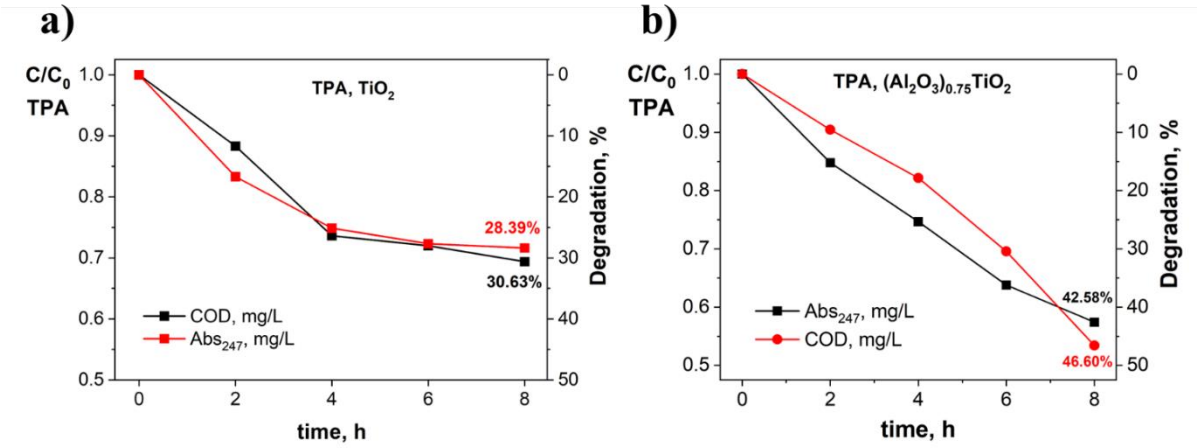

Figure 8. Photocatalytic degradation of TPA with a) TiO_2 and b) $(Al_2O_3)_{0.75}TiO_2$ coatings.

The degradation efficiency of TPA with $(Al_2O_3)_{0.75}TiO_2$ in 8 h, which lasted the reaction study, was 42.58%, measured by absorbance at 247 nm and 46.60%, measured as COD with the difference of 9.4% (Figure 8b).

First pseudo first order kinetics were observed with a rate constant of k_{cat}=0.047 h^{-1}. The catalysis rate constant was k_{cat}=0.0697 h^{-1}, above the efficiency shown with the TiO_2 coating with the difference that it was achieved after 8 h (Figure 9a).

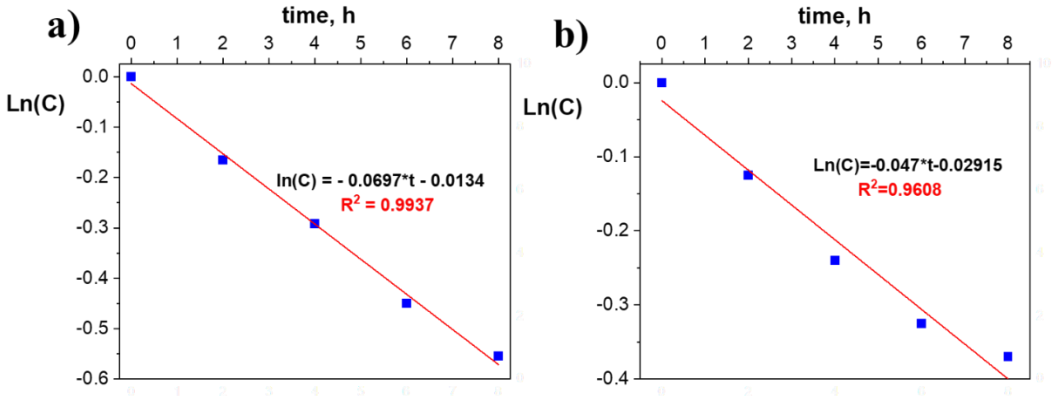

Figure 9. Photocatalytic degradation kinetics of TPA, a) TiO_2, and b) $(Al_2O_3)_{0.75}TiO_2$ coatings.

The efficiency of the $(Al_2O_3)_{0.75}TiO_2$ system increases, because the excited electrons in the valence band of TiO_2 are transferred to the amphoteric Al_2O_3, which acts as an electron sink (cocatalyst) leading to photogenerated holes on the surface of rutile/anatase TiO_2. The reduction of the h^+/e^- pair recombination triggers the dissociation of a water molecule, producing hydroxyl radicals, and under predominating basic conditions, the oxidation-reduction reactions are boosted to degrade TPA (Ali et al., 2018; Miwa et al., 2010).

3.3. Evaluation of the Photocatalytic Efficiency of PET Degradation by the Immobilized $(Al_2O_3)_{0.75}TiO_2$ System

The UV-visible spectroscopy analysis of PET shows at t_0=0 only two broad bands within the 203-207 nm interval, where the n→π^* transitions of carboxyl (-COO-) and -OH- groups present in polyethylene terephthalate are commonly found (Figure 10). The other broad band between 208-213 nm is characterized by the π→π^* transitions of the sp^2 C=C conjugated bonds of the aromatic ring and the bond occurring with a sp^2 carbon.

 doi:10.20944/preprints202503.2121.v1

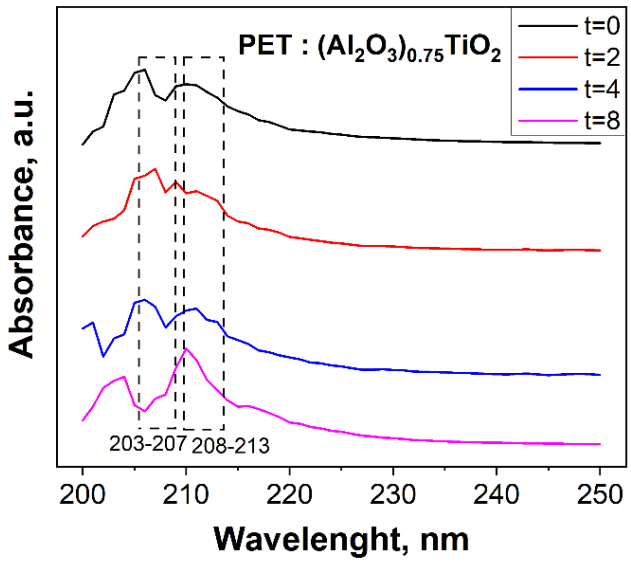

Figure 10. UV-visible analysis of PET structural changes by heterogeneous photocatalysis by $(Al_2O_3)_{0.75}TiO_2$.

In PET, the carboxyl groups of terephthalate and OH groups of ethylene glycol are linked together by an ester bond (203-207 nm), while the repeating structural unit has, in addition to ester bonds, Csp^3-Csp^2 covalent bonds (208-213 nm). The attack of hydroxyl radicals on the ester bonds progresses the depolymerization reaction, causing the linking of the n repeating units of PET and the formation of n units of mono 2-hydroxyethyl terephthalate (MHET), consequently PET precursors: TPA and ethylene glycol. The decrease in the intensity of the absorption band of the ester bond between 203-207 nm and the appearance of the band at 201 nm characteristic of free carboxyl groups, confirm the results (Tawfik & Eskander, 2015). The ethylene glycol molecule could be easily mineralized to CO_2 and H_2O by biological means. In addition, several studies that have addressed the microbial bioremediation of PET by various microbial consortia refer to its transformation into mono (2-hydroxyethyl) terephthalic acid (MHET) by the extracellular enzyme PETase. MHET passes to the periplasmic region of the microorganisms, where it is transformed by the enzyme MHETase into terephthalic acid and ethylene glycol (Kulkarni et al., 2024). Such mechanism agrees with the analysis of the UV-Vis spectra of heterogeneous photocatalysis by the $(Al_2O_3)_{0.75}TiO_2$ system with the advantage that no strict control favoring enzymatic activity is necessary for PET biodegradation.

Figure 11 shows that the degradation efficiency of PET was 37.03%, measured by absorbance at 210 nm, and 41.18%, measured as COD; in both cases, a continuous degradation trend is observed that can continue for more than 8 h until obtaining degradation equal to or greater than 50% of PET.

According to the test, pseudo first order kinetics is observed with a photocatalysis rate constant of k_{cat}=0.0534 h^{-1}. Following pseudo first order kinetics, 50% degradation of PET would occur in a period of approximately 13 h, which is equivalent to the half-life of the reaction. (Figure 11 b).

 doi:10.20944/preprints202503.2121.v1

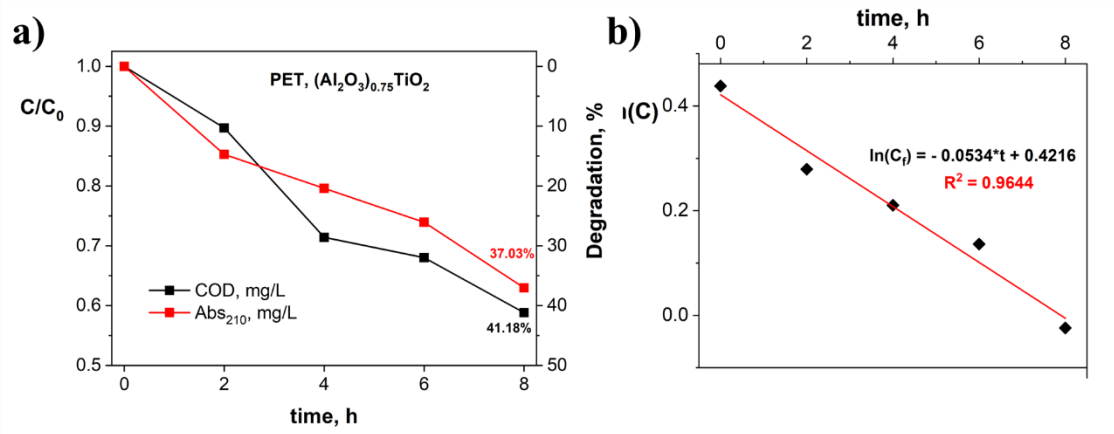

Figure 11. a) Photocatalytic degradation of PET, $(Al_2O_3)_{0.75}TiO_2$ coating; b) degradation kinetics.

4. Conclusions

The selection of TPA and PET contaminants was done because TPA is the hydrolysis product of PET, PET can be degraded to TPA and the latter can also be degraded to less toxic contaminants, which represents a challenge for water treatment technology. The reduction of the COD measurement for an initial TPA concentration of 50 mg/L in the reactor with the modified arrangement of stainless-steel discs with the $(Al_2O_3)_{0.75}TiO_2$ coating and lamps reached 46.60%. This kind of reduction could be associated with the low-scale formation of CO_2 from the TPA carboxyl groups. The UV-Vis analysis for 8 h of determination shows the splitting of initial bands those results in the formation of intermediate products. Commercial PET sampling in the presence of the immobilized $(Al_2O_3)_{0.75}TiO_2$ photocatalyst reduced the COD value to 41% and the UV-Vis analysis revealed degradation efficiency of 37%.

References

1. Agostini, I., Ciuffi, B., Gallorini, R., Rizzo, A. M., Chiaramonti, D., & Rosi, L. (2022). Recovery of Terephthalic Acid from Densified Post-consumer Plastic Mix by HTL Process. In *Molecules* (Vol. 27, Issue 20). https://doi.org/10.3390/molecules27207112
2. Al Miad, A., Saikat, S. P., Alam, M. K., Sahadat Hossain, M., Bahadur, N. M., & Ahmed, S. (2024). Metal oxide-based photocatalysts for the efficient degradation of organic pollutants for a sustainable environment: a review. *Nanoscale Advances*, *6*(19), 4781–4803. https://doi.org/https://doi.org/10.1039/d4na00517a
3. Ali, I., Suhail, M., Alothman, Z. A., & Alwarthan, A. (2018). Recent advances in syntheses, properties and applications of TiO2 nanostructures. *RSC Advances*, *8*(53), 30125–30147. https://doi.org/10.1039/C8RA06517A
4. Askeland, D. R., & Wright, W. J. (1998). *Ciencia e ingeniería de los materiales* (Vol. 3). International Thomson Editores México.
5. Barajas-Ledesma, E., García-Benjume, M. L., Espitia-Cabrera, I., Ortiz-Gutiérrez, M., Espinoza-Beltrán, F. J., Mostaghimi, J., & Contreras-García, M. E. (2010). Determination of the band gap of TiO2–Al2O3 films as a function of processing parameters. *Materials Science and Engineering: B*, *174*(1), 71–73. https://doi.org/https://doi.org/10.1016/j.mseb.2010.05.001
6. Billings, A., Jones, K. C., Pereira, M. G., & Spurgeon, D. J. (2021). Plasticisers in the terrestrial environment: sources, occurrence and fate. *Environmental Chemistry*, *18*(3), 111–130. https://doi.org/10.1071/EN21033
7. Brinker, C. J., & Scherer, G. W. (2013). Sol-gel science: the physics and chemistry of sol-gel processing. Academic press.
8. Byrne, C., Subramanian, G., & Pillai, S. C. (2018). Recent advances in photocatalysis for environmental applications. *Journal of Environmental Chemical Engineering*, *6*(3), 3531–3555. https://doi.org/https://doi.org/10.1016/j.jece.2017.07.080

 doi:10.20944/preprints202503.2121.v1

9. Camacho-González, M. A., Lijanova, I. V, Reyes-Miranda, J., Sarmiento-Bustos, E., Quezada-Cruz, M., Vera-Serna, P., Barrón-Meza, M. Á., & Garrido-Hernández, A. (2023). High Photocatalytic Efficiency of Al2O3-TiO2 Coatings on 304 Stainless Steel for Methylene Blue and Wastewater Degradation. In *Catalysts* (Vol. 13, Issue 10). https://doi.org/10.3390/catal13101351
10. Chang, B. V, Yang, C. M., Cheng, C. H., & Yuan, S. Y. (2004). Biodegradation of phthalate esters by two bacteria strains. *Chemosphere*, *55*(4), 533–538. https://doi.org/https://doi.org/10.1016/j.chemosphere.2003.11.057
11. da Trindade, C. de M., da Silva, S. W., Bortolozzi, J. P., Banús, E. D., Bernardes, A. M., & Ulla, M. A. (2018). Synthesis and characterization of TiO2 films onto AISI 304 metallic meshes and their application in the decomposition of the endocrine-disrupting alkylphenolic chemicals. *Applied Surface Science*, *457*, 644–654. https://doi.org/https://doi.org/10.1016/j.apsusc.2018.06.287
12. Duan, L., Wang, B., Heck, K., Guo, S., Clark, C. A., Arredondo, J., Wang, M., Senftle, T. P., Westerhoff, P., Wen, X., Song, Y., & Wong, M. S. (2020). Efficient Photocatalytic PFOA Degradation over Boron Nitride. *Environmental Science & Technology Letters*, *7*(8), 613–619. https://doi.org/10.1021/acs.estlett.0c00434
13. Fang, P., Liu, B., Xu, J., Zhou, Q., Zhang, S., Ma, J., & lu, X. (2018). High-efficiency glycolysis of poly(ethylene terephthalate) by sandwich-structure polyoxometalate catalyst with two active sites. *Polymer Degradation and Stability*, *156*, 22–31. https://doi.org/https://doi.org/10.1016/j.polymdegradstab.2018.07.004
14. Farhadian Azizi, K., & Bagheri-Mohagheghi, M.-M. (2013). Transition from anatase to rutile phase in titanium dioxide (TiO2) nanoparticles synthesized by complexing sol–gel process: effect of kind of complexing agent and calcinating temperature. *Journal of Sol-Gel Science and Technology*, *65*(3), 329–335. https://doi.org/10.1007/s10971-012-2940-2
15. Gogate, P. R., & Pandit, A. B. (2004). A review of imperative technologies for wastewater treatment II: hybrid methods. *Advances in Environmental Research*, *8*(3), 553–597. https://doi.org/https://doi.org/10.1016/S1093-0191(03)00031-5
16. Habibi, S., & Jamshidi, M. (2020). Sol–gel synthesis of carbon-doped TiO2 nanoparticles based on microcrystalline cellulose for efficient photocatalytic degradation of methylene blue under visible light. *Environmental Technology*, *41*(24), 3233–3247. https://doi.org/10.1080/09593330.2019.1604815
17. Huang, Z., Zhao, S., & Yu, Y. (2020). Experimental method to explore the adaptation degree of type-II and all-solid-state Z-scheme heterojunction structures in the same degradation system. *Chinese Journal of Catalysis*, *41*(10), 1522–1534. https://doi.org/https://doi.org/10.1016/S1872-2067(19)63495-9
18. Ibarra, I. C. R., Dubé, I. Z., & Sánchez, M. F. G. (2020). 1. MX2019002787 - Reactor fotocatalítico para la degradación de contaminantes orgánicos a presiones por encima de los valores ambientales (Patent No. 2019002787). 2019002787. https://www.wipo.int/ipcpub/?symbol=B01J0003000000&menulang=es&lang=es
19. Jiang, Q., Liu, J., Qi, T., & Liu, Y. (2022). Enhanced visible-light photocatalytic activity and antibacterial behaviour on fluorine and graphene synergistically modified TiO2 nanocomposite for wastewater treatment. *Environmental Technology*, *43*(25), 3821–3834. https://doi.org/10.1080/09593330.2021.1936198
20. Kamari, H. M., Al-Hada, N. M., Baqer, A. A., Shaari, A. H., & Saion, E. (2019). Comprehensive study on morphological, structural and optical properties of Cr2O3 nanoparticle and its antibacterial activities. *Journal of Materials Science: Materials in Electronics*, *30*(8), 8035–8046. https://doi.org/10.1007/s10854-019-01125-2
21. Kanakaraju, D., Motti, C. A., Glass, B. D., & Oelgemöller, M. (2014). Photolysis and TiO2-catalysed degradation of diclofenac in surface and drinking water using circulating batch photoreactors. *Environmental Chemistry*, *11*(1), 51–62. https://doi.org/10.1071/EN13098
22. Kaneco, S., Rahman, M. A., Suzuki, T., Katsumata, H., & Ohta, K. (2004). Optimization of solar photocatalytic degradation conditions of bisphenol A in water using titanium dioxide. *Journal of Photochemistry and Photobiology A: Chemistry*, *163*(3), 419–424. https://doi.org/https://doi.org/10.1016/j.jphotochem.2004.01.012
23. Karunakaran, C., Magesan, P., Gomathisankar, P., & Vinayagamoorthy, P. (2015). Absorption, emission, charge transfer resistance and photocatalytic activity of Al2O3/TiO2 core/shell nanoparticles. *Superlattices and Microstructures*, *83*, 659–667. https://doi.org/https://doi.org/10.1016/j.spmi.2015.04.014

 doi:10.20944/preprints202503.2121.v1

24. Kleerebezem, R., Beckers, J., Hulshoff Pol, L. W., & Lettinga, G. (2005). High rate treatment of terephthalic acid production wastewater in a two-stage anaerobic bioreactor. *Biotechnology and Bioengineering*, *91*(2), 169–179. https://doi.org/10.1002/bit.20502
25. Kolesnik, O. (2024). UV-Vis Spectrum of Terephthalic acid. *SIELC Technologies*. https://sielc.com/uv-vis-spectrum-of-terephthalic-acid
26. Krishnan, A., Swarnalal, A., Das, D., Krishnan, M., Saji, V. S., & Shibli, S. M. A. (2024). A review on transition metal oxides based photocatalysts for degradation of synthetic organic pollutants. *Journal of Environmental Sciences*, *139*, 389–417. https://doi.org/https://doi.org/10.1016/j.jes.2023.02.051
27. Kulkarni, R. M., Patwardhan, N. S., Iyer, P. B., & Bharadwaj, T. D. (2024). A review on microbial bioremediation of polyethylene terephthalate microplastics. *Environmental Quality Management*, *34*(2), e22264.
28. Kurokawa, H., Ohshima, M., Sugiyama, K., & Miura, H. (2003). Methanolysis of polyethylene terephthalate (PET) in the presence of aluminium tiisopropoxide catalyst to form dimethyl terephthalate and ethylene glycol. *Polymer Degradation and Stability*, *79*(3), 529–533. https://doi.org/https://doi.org/10.1016/S0141-3910(02)00370-1
29. Li, H., Zhang, W., Xia, D., Ye, L., Ma, W., Li, H., Li, Q., & Wang, Y. (2022). Improved anaerobic degradation of purified terephthalic acid wastewater by adding nanoparticles or co-substrates to facilitate the electron transfer process. *Environmental Science: Nano*, *9*(3), 1011–1024. https://doi.org/10.1039/D1EN01037A
30. Liu, X., Iocozzia, J., Wang, Y., Cui, X., Chen, Y., Zhao, S., Li, Z., & Lin, Z. (2017). Noble metal–metal oxide nanohybrids with tailored nanostructures for efficient solar energy conversion, photocatalysis and environmental remediation. *Energy & Environmental Science*, *10*(2), 402–434. https://doi.org/10.1039/C6EE02265K
31. Liu, X., Wan, Y., & Zhang, X. (2023). Preparation and Corrosion Properties of TiO2-SiO2-Al2O3 Composite Coating on Q235 Carbon Steel. In *Coatings* (Vol. 13, Issue 12). https://doi.org/10.3390/coatings13121994
32. Luo, H., Xiang, Y., Tian, T., & Pan, X. (2021). An AFM-IR study on surface properties of nano-TiO2 coated polyethylene (PE) thin film as influenced by photocatalytic aging process. *Science of The Total Environment*, *757*, 143900. https://doi.org/https://doi.org/10.1016/j.scitotenv.2020.143900
33. Ma, K., Li, X., Bao, L., Li, X., & Cui, Y. (2020). The performance and bacterial community shifts in an anaerobic-aerobic process treating purified terephthalic acid wastewater under influent composition variations and ambient temperatures. *Journal of Cleaner Production*, *276*, 124190. https://doi.org/https://doi.org/10.1016/j.jclepro.2020.124190
34. Ma, X., Li, X., Wang, X., Liu, G., Zuo, J., Wang, S., & Wang, K. (2020). Impact of salinity on anaerobic microbial community structure in high organic loading purified terephthalic acid wastewater treatment system. *Journal of Hazardous Materials*, *383*, 121132. https://doi.org/https://doi.org/10.1016/j.jhazmat.2019.121132
35. Magnone, E., Kim, M. K., Lee, H. J., & Park, J. H. (2021). Facile synthesis of TiO2-supported Al2O3 ceramic hollow fiber substrates with extremely high photocatalytic activity and reusability. *Ceramics International*, *47*(6), 7764–7775. https://doi.org/https://doi.org/10.1016/j.ceramint.2020.11.121
36. Mahmoodi, N. M., & Arami, M. (2006). Bulk phase degradation of Acid Red 14 by nanophotocatalysis using immobilized titanium(IV) oxide nanoparticles. *Journal of Photochemistry and Photobiology A: Chemistry*, *182*(1), 60–66. https://doi.org/https://doi.org/10.1016/j.jphotochem.2006.01.014
37. Martinez-Gómez, C., Rangel-Vazquez, I., Zarraga, R., del Ángel, G., Ruíz-Camacho, B., Tzompantzi, F., Vidal-Robles, E., & Perez-Larios, A. (2022). Photodegradation and Mineralization of Phenol Using TiO2Coated γ-Al2O3: Effect of Thermic Treatment. In *Processes* (Vol. 10, Issue 6). https://doi.org/10.3390/pr10061186
38. Mazzarino, I., & Piccinini, P. (1999). Photocatalytic oxidation of organic acids in aqueous media by a supported catalyst. *Chemical Engineering Science*, *54*(15), 3107–3111. https://doi.org/https://doi.org/10.1016/S0009-2509(98)00430-8
39. Merino, N., Qu, Y., Deeb, R. A., Hawley, E. L., Hoffmann, M. R., & Mahendra, S. (2016). Degradation and Removal Methods for Perfluoroalkyl and Polyfluoroalkyl Substances in Water. *Environmental Engineering Science*, *33*(9), 615–649. https://doi.org/10.1089/ees.2016.0233

 doi:10.20944/preprints202503.2121.v1

40. Miglierini, M. B., Pašteka, L., Cesnek, M., Kmječ, T., Bujdoš, M., & Kohout, J. (2019). Influence of surface treatment on microstructure of stainless steels studied by Mössbauer spectrometry. *Journal of Radioanalytical and Nuclear Chemistry*, *322*(3), 1495–1503. https://doi.org/10.1007/s10967-019-06737-w
41. Miwa, T., Kaneco, S., Katsumata, H., Suzuki, T., Ohta, K., Chand Verma, S., & Sugihara, K. (2010). Photocatalytic hydrogen production from aqueous methanol solution with CuO/Al2O3/TiO2 nanocomposite. *International Journal of Hydrogen Energy*, *35*(13), 6554–6560. https://doi.org/https://doi.org/10.1016/j.ijhydene.2010.03.128
42. Muñoz Sierra, J. D., Lafita, C., Gabaldón, C., Spanjers, H., & van Lier, J. B. (2017). Trace metals supplementation in anaerobic membrane bioreactors treating highly saline phenolic wastewater. *Bioresource Technology*, *234*, 106–114. https://doi.org/https://doi.org/10.1016/j.biortech.2017.03.032
43. Mwema, F. M., Oladijo, O. P., Sathiaraj, T. S., & Akinlabi, E. T. (2018). Atomic force microscopy analysis of surface topography of pure thin aluminum films. *Materials Research Express*, *5*(4), 46416. https://doi.org/10.1088/2053-1591/aabe1b
44. Oladijo, O. P., Popoola, A. P. I., Booi, M., Fayomi, J., & Collieus, L. L. (2020). Corrosion and mechanical behaviour of Al2O3TiO2 composites produced by spark plasma sintering. *South African Journal of Chemical Engineering*, *33*, 58–66. https://doi.org/https://doi.org/10.1016/j.sajce.2020.05.001
45. Park, T.-J., Lim, J. S., Lee, Y.-W., & Kim, S.-H. (2003). Catalytic supercritical water oxidation of wastewater from terephthalic acid manufacturing process. *The Journal of Supercritical Fluids*, *26*(3), 201–213. https://doi.org/https://doi.org/10.1016/S0896-8446(02)00161-4
46. Peng, Y., Yang, J., Deng, C., Deng, J., Shen, L., & Fu, Y. (2023). Acetolysis of waste polyethylene terephthalate for upcycling and life-cycle assessment study. *Nature Communications*, *14*(1), 3249. https://doi.org/10.1038/s41467-023-38998-1
47. Radoń, A., Drygała, A., Hawełek, Ł., & Łukowiec, D. (2017). Structure and optical properties of Fe3O4 nanoparticles synthesized by co-precipitation method with different organic modifiers. *Materials Characterization*, *131*, 148–156. https://doi.org/https://doi.org/10.1016/j.matchar.2017.06.034
48. Ran, Y., Zhong, J., Li, J., Li, M., & Tian, C. (2023). Substantially boosted photocatalytic detoxification activity of TiO2 benefited from Eu doping. *Environmental Technology*, *44*(9), 1313–1321. https://doi.org/10.1080/09593330.2021.2000041
49. Sacco, O., Vaiano, V., Rizzo, L., & Sannino, D. (2018). Photocatalytic activity of a visible light active structured photocatalyst developed for municipal wastewater treatment. *Journal of Cleaner Production*, *175*, 38–49. https://doi.org/https://doi.org/10.1016/j.jclepro.2017.11.088
50. Sadeq, Z. S., Mahdi, Z. F., & Hamza, A. M. (2019). Low cost, fast and powerful performance interfacial charge transfer nanostructured Al2O3 capturing of light photocatalyst eco-friendly system using hydrothermal method. *Materials Letters*, *254*, 120–124. https://doi.org/https://doi.org/10.1016/j.matlet.2019.07.050
51. Samy, M., Ibrahim, M. G., Fujii, M., Diab, K. E., ElKady, M., & Gar Alalm, M. (2021). CNTs/MOF-808 painted plates for extended treatment of pharmaceutical and agrochemical wastewaters in a novel photocatalytic reactor. *Chemical Engineering Journal*, *406*, 127152. https://doi.org/https://doi.org/10.1016/j.cej.2020.127152
52. Sannino, D., Vaiano, V., Sacco, O., Morante, N., Guglielmo, L. De, Capua, G. Di, & Femia, N. (2021). Visible Light Driven Degradation of Terephthalic Acid: Optimization of Energy Demand by Light Modulation Techniques. In *Journal of Photocatalysis* (Vol. 2, Issue 1, pp. 49–61). https://doi.org/http://dx.doi.org/10.2174/2665976X01999200731185927
53. Shafaei, A., Nikazar, M., & Arami, M. (2010). Photocatalytic degradation of terephthalic acid using titania and zinc oxide photocatalysts: Comparative study. *Desalination*, *252*(1), 8–16. https://doi.org/https://doi.org/10.1016/j.desal.2009.11.008
54. Skoog, D. A., Holler, F. J., & Crouch, S. R. (2008). Principios de Análisis Instrumental (sexta edición ed.). *Cengage Learning*.
55. Sun, Y., Tian, L., Liu, B., Chen, F., & Ge, S. (2021). Photocatalytic Destruction of Gaseous Benzene Using Mn/I-Doped TiO2 Nanoparticle Catalytic Under Visible Light. *Environmental Engineering Science*, *39*(3), 259–267. https://doi.org/10.1089/ees.2021.0093

 doi:10.20944/preprints202503.2121.v1

56. Tawfik, M., & Eskander, S. (2015). Recycling of Polyethylene Terephthalate Plastic Wastes based on unsaturated Diol. *KGK Rubberpoint*, *68*, 21–27.
57. Thiruvenkatachari, R., Kwon, T. O., Jun, J. C., Balaji, S., Matheswaran, M., & Moon, I. S. (2007). Application of several advanced oxidation processes for the destruction of terephthalic acid (TPA). *Journal of Hazardous Materials*, *142*(1), 308–314. https://doi.org/https://doi.org/10.1016/j.jhazmat.2006.08.023
58. Tian, L., Alizadeh, A. A., Gentles, A. J., & Tibshirani, R. (2014). A Simple Method for Estimating Interactions between a Treatment and a Large Number of Covariates. *Journal of the American Statistical Association*, *109*(508), 1517–1532. https://doi.org/10.1080/01621459.2014.951443
59. Wang, Y., Xu, M., Li, J., & Zhang, T. (2024). Photocatalytic Degradation of Organic Pollutants Using Al/TiO2 Composites Under Visible Light. *Environmental Engineering Science*, *41*(5), 204–215. https://doi.org/10.1089/ees.2023.0313
60. Xiao, Y., Luo, W. P., Zhang, X. Y., Guo, C. C., Liu, Q., Jiang, G. F., & Li, Q. H. (2010). Aerobic Oxidation of p-Toluic Acid to Terephthalic Acid over T(p-Cl)PPMnCl/Co(OAc)2 Under Moderate Conditions. *Catalysis Letters*, *134*(1), 155–161. https://doi.org/10.1007/s10562-009-0227-1
61. Xu, L., Song, H., & Chou, L. (2012). Facile synthesis of nano-crystalline alpha-alumina at low temperature via an absolute ethanol sol–gel strategy. *Materials Chemistry and Physics*, *132*(2), 1071–1076. https://doi.org/https://doi.org/10.1016/j.matchemphys.2011.12.069
62. Yakdoumi, F. Z., & Hadj-Hamou, A. S. (2020). Effectiveness assessment of TiO_2-Al_2O_3 nano-mixture as a filler material for improvement of packaging performance of PLA nanocomposite films. *Journal of Polymer Engineering*, *40*(10), 848–858. https://doi.org/10.1515/polyeng-2020-0105
63. Yan, J., Cheng, S. P., Zhang, X. X., Shi, L., & Zhu, C. J. (2004). Effects of Four Metals on the Degradation of Purified Terephthalic Acid Wastewater by Phanerochaete chrysosporium and Strain Fhhh. *Bulletin of Environmental Contamination and Toxicology*, *72*(2), 387–393. https://doi.org/10.1007/s00128-003-8880-3
64. Žerjav, G., Albreht, A., Vovk, I., & Pintar, A. (2020). Revisiting terephthalic acid and coumarin as probes for photoluminescent determination of hydroxyl radical formation rate in heterogeneous photocatalysis. *Applied Catalysis A: General*, *598*, 117566. https://doi.org/https://doi.org/10.1016/j.apcata.2020.117566
65. Zhang, H., Wu, J., Li, R., Kim, D.-H., Bi, X., Zhang, G., Jiang, B., Yong Ng, H., & Shi, X. (2022). Novel intertidal wetland sediment-inoculated moving bed biofilm reactor treating high-salinity wastewater: Metagenomic sequencing revealing key functional microorganisms. *Bioresource Technology*, *348*, 126817. https://doi.org/https://doi.org/10.1016/j.biortech.2022.126817
66. Zhang, Q., Li, R., Li, Z., Li, A., Wang, S., Liang, Z., Liao, S., & Li, C. (2016). The dependence of photocatalytic activity on the selective and nonselective deposition of noble metal cocatalysts on the facets of rutile TiO2. *Journal of Catalysis*, *337*, 36–44. https://doi.org/https://doi.org/10.1016/j.jcat.2016.01.001
67. Zhang, W., Li, Y., Wu, Q., & Hu, H. (2011). Removal of Endocrine-Disrupting Compounds, Estrogenic Activity, and Escherichia coliform from Secondary Effluents in a TiO2-Coated Photocatalytic Reactor. *Environmental Engineering Science*, *29*(3), 195–201. https://doi.org/10.1089/ees.2010.0387
68. Zhang, X., Yang, S., Li, J., & Wu, J. (2020). Temperature-dependent evolution of oxide inclusions during heat treatment of stainless steel with yttrium addition. *International Journal of Minerals, Metallurgy and Materials*, *27*(6), 754–763. https://doi.org/10.1007/s12613-019-1935-1
69. Zhu, L., Lu, Q., Lv, L., Wang, Y., Hu, Y., Deng, Z., Lou, Z., Hou, Y., & Teng, F. (2017). Ligand-free rutile and anatase TiO2 nanocrystals as electron extraction layers for high performance inverted polymer solar cells. *RSC Advances*, *7*(33), 20084–20092. https://doi.org/10.1039/C7RA00134G
70. Zhu, Y., Ning, Y., Li, L., Chen, Z., Li, H., & Zhang, Y. (2022). Effective removal of hexavalent chromium from aqueous system by biochar-supported titanium dioxide (TiO2). *Environmental Chemistry*, *19*(7), 432–445. https://doi.org/10.1071/EN22092
71. Zielińska-Jurek, A., Wysocka, I., Janczarek, M., Stampor, W., & Hupka, J. (2015). Preparation and characterization of Pt–N/TiO2 photocatalysts and their efficiency in degradation of recalcitrant chemicals. *Separation and Purification Technology*, *156*, 369–378. https://doi.org/https://doi.org/10.1016/j.seppur.2015.10.024

 doi:10.20944/preprints202503.2121.v1